Selective and energy-efficient electrosynthesis of ethylene from CO2 by tuning the valence of Cu catalysts through aryl diazonium functionalization

Huali Wu, Lingqi Huang, Janis Timoshenko, Kun Qi, Wensen Wang, Jiefeng Liu, Yang Zhang, Shaokang Yang, Eddy Petit, Valérie Flaud, et al.

▶ **To cite this version:**

Huali Wu, Lingqi Huang, Janis Timoshenko, Kun Qi, Wensen Wang, et al.. Selective and energy-efficient electrosynthesis of ethylene from CO2 by tuning the valence of Cu catalysts through aryl diazonium functionalization. Nature Energy, 2024, 9 (4), pp.422-433. ⟨10.1038/s41560-024-01461-6⟩. ⟨hal-04747870⟩

HAL Id: hal-04747870

https://hal.science/hal-04747870v1

Submitted on 22 Oct 2024

HAL is a multi-disciplinary open access archive for the deposit and dissemination of scientific research documents, whether they are published or not. The documents may come from teaching and research institutions in France or abroad, or from public or private research centers.

L'archive ouverte pluridisciplinaire **HAL**, est destinée au dépôt et à la diffusion de documents scientifiques de niveau recherche, publiés ou non, émanant des établissements d'enseignement et de recherche français ou étrangers, des laboratoires publics ou privés.

HAL Authorization

Selective and energy-efficient electrosynthesis of ethylene *via* valence engineering of the Cu sites

Huali Wu[1], Lingqi Huang[2], Janis Timoshenko[3], Kun Qi[1], Wensen Wang[1], Jiefeng Liu[1], Yang Zhang[1], Shaokang Yang[4], Eddy Petit[1], Valérie Flaud[5], Ji Li[6], Chrystelle Salameh[1], Philippe Miele[1,7], Luc Lajaunie[8,9], Beatriz Roldán Cuenya[3], Dewei Rao*[4], Damien Voiry*[1]

[1] *Institut Européen des Membranes, IEM, UMR 5635, Université Montpellier, ENSCM, CNRS, Montpellier 34000, France*

[2] *School of Science and Engineering, The Chinese University of Hong Kong, Shenzhen, Guangdong, 518172, PR China*

[3] *Department of Interface Science, Fritz-Haber-Institute of the Max-Planck Society, 14195 Berlin, Germany*

[4] *School of Materials Science and Engineering, Jiangsu University, Zhenjiang, 212013, PR China*

[5] *Institut Charles Gerhardt, ICGM, UMR 5253, University of Montpellier, ENSCM, CNRS, 34095 Montpellier Cedex5, France*

[6] *College of Bioresources and Materials Engineering, Shanxi University of Science & Technology, Xi'an 710021, PR China*

[7] *Institut Universitaire de France (IUF), 1 rue Descartes, 75231 Paris Cedex 05*

[8] *Departamento de Ciencia de los Materiales e Ingeniería Metalúrgica y Química Inorgánica, Facultad de Ciencias, Universidad de Cádiz, Campus Río San Pedro S/N, Puerto Real, 11510, Cádiz, Spain*

[9] *Instituto Universitario de Investigación de Microscopía Electrónica y Materiales (IMEYMAT), Facultad de Ciencias, Universidad de Cádiz, Campus Río San Pedro S/N, Puerto Real 11510, Cádiz, Spain*

Abstract

The electrosynthesis of ethylene (C_2H_4) in membrane-electrode-assembly (MEA) cells with high selectivity and large current density is a promising flow process strategy for the conversion of CO_2 or CO into valuable products. Although considerable progress has been made in meeting industrial requirements in terms of Faradaic efficiency (FE) and formation rate, selectivity towards the formation of a single type of multi-carbon (C_{2+}) product has not been demonstrated to date. Here, we evaluated a library of aryl diazonium salts to functionalize Cu catalysts in order to elucidate the influence of Cu valence on the formation of multi-carbon products during the CO_2RR. By combining density functional theory (DFT) calculations with *operando* Raman and X-ray absorption spectroscopy (XAS), we identified the role of the surface oxidation state of $Cu^{\delta+}$ with $0<\delta<1$ on the selectivity and the formation rate of C_2H_4. As a result, we report a FE and a specific current density for C_2H_4 as large as 83±2% and 212 mA cm^{-2}, respectively on partially oxidized $Cu^{0.26+}$. This corresponds to an energy efficiency of 26.9% and an electrical power consumption (EPC) of 61.4 kWh $N^{-1}m^{-3}$. The conversion performance was further improved by using a perfluorinated sulfonic acid (PFSA) ionomer to reach a record-high FE for C_2H_4 of 89±3% at a specific current density of 536 mA cm^{-2}. When coupled with an Ag-based MEA cell to generate CO from CO_2 in a cascade flow process, an energy efficiency of ~40 % with a FE_{C2H4} of 86± 2% was achieved, corresponding to a record low EPC of 25.6 kWh $N^{-1}m^{-3}$.

Introduction

The global consumption of fossil fuels induces profound environmental repercussions and is responsible for colossal emission of > 35 Gt of CO_2 every year. The pledge of net zero emission

by 2050 requires the development of economically viable technologies to reuse the emitted CO_2 and close the carbon cycle. The electrochemical CO_2 reduction reaction (CO_2RR) provides a promising and sustainable route to convert CO_2 into valuable chemicals and fuels when powered by renewable electricity[1,2]. Ethylene has been identified as a desirable multi-carbon product of the CO_2RR owing to its high commercial value and large market size with an annual global production of 140 million metric tons and a market value of 182 billion USD[3]. Techno-economic analyses (TEA) emphasized the necessity to operate CO_2RR at specific current densities larger than 200 mA cm^{-2} while minimizing the power input (or cell voltage)[4]. Although the best reported performance of electrocatalysis of CO_2 to ethylene in liquid flow cells meets industrial requirements with specific current densities >900 mA cm^{-2} for ethylene, the stability remains insufficient to compete with traditional ethylene production from fossil sources as well as bio-based ethylene[3,5-9](Supplementary Fig. 1 and Supplementary Table 1).

Zero-gap membrane electrode assembly (MEA) cells, comprising a cathode, membrane, and anode, offer the potential to achieve industry-relevant current densities with high selectivity and formation rates, while the continuous flow process provides a large mass transfer boundary layer with high local CO_2 concentration near the planar electrodes[10-12]. The absence of catholyte makes MEA cells more stable than traditional liquid flow cells by mitigating the electrode flooding and the precipitation of salts, resulting in greater operating stability and reduced operational expenses (OPEX)[12,13]. The exploitation of MEA cells with high selectivity and high current density for the ethylene production as well as prolonged stability, is thus expected to lower the threshold of economic viability to replace fossil sources for ethylene production. To date, the selectivity and the specific current density for ethylene in MEA systems are however limited to <80% and < 200 mA cm^{-2} (Refs.[6,14]).

It has been reported that partially oxidized copper sites: $Cu^{\delta+}$, $0<\delta<1$ facilitate the conversion of CO_2 to C_{2+} products by decreasing the energy barrier associated with the CO dimerization and the formation of *OCCOH intermediate[15-19]. Investigations of the role of $Cu^{\delta+}$ proved to be tedious, while the intrinsic instability of $Cu^{\delta+}$ species, especially at high cathodic potentials,

leads to a rapid loss of performance[20]. Recent studies have emphasized the importance of controlling the oxidation state of Cu sites and the presence of Cu^+ species on the electrode surface for efficient CO_2 reduction. Various approaches, such as controlled oxidation, pulse polarization, or molecular doping, have been explored to achieve this goal[6,12,17].

Aryl diazonium salts are well-known electrophiles that have been extensively used for covalent surface modification since their first demonstration[21-26]. The strong interfacial bonding of aryl groups with the metal surface, which is covalent in nature, makes it much stable and widely applied in various fields[21,26-28], including biosensors' development[29-31], antibacterial activity and drug delivery[29,32,33]. The electron withdrawing ability of the aryl group can be adjusted by the nature of the substituents. We hypothesize that the covalent binding of aryl groups onto the Cu surface results in stable valence, making aryl diazonium salts an attractive choice for fine-tuning the valence of surface Cu atoms[21,24,26,28].

Herein, we report a functionalization strategy based on aryl diazonium salts used as electrophile reagents with a strong affinity for electron-rich copper metal. We identified that the nature of different substituted aryl groups can precisely tailor the oxidation state of surface Cu sites as confirmed by our density functional theory (DFT) calculations. We predict that controlled doping of Cu can facilitate C-O bond breaking followed by C-H hydrogenation of the $*CH_2CHOH$ intermediate, which favors the selective formation of ethylene (C_2H_4) over ethanol (C_2H_5OH) during the CO_2RR. We corroborated the DFT results by integrating the aryl functionalized catalysts into an MEA flow cell. By tailoring the valence of the Cu sites, we achieved a FE_{C2H4} of 83% at a current density of 212 mA cm^{-2} for the electrosynthesis of ethylene from CO_2 with an optimal oxidation state for Cu of +0.26. This corresponds to a ~200% increase of the ethylene formation rate compared to the pristine Cu and a C_2H_4 *vs.* C_2+ selectivity greater than 97% and a sustained stability for 120 hours. When fed with CO, the MEA cell demonstrated a FE for C_2H_4 of ~86% with a full cell energy efficiency of ~40 %, setting a new benchmark for the formation of ethylene from CO.

Density functional theory calculations

We first carried out Bader charge analysis to assess how the electron-withdrawing capability of the aryl groups influences the valence of Cu. Our findings revealed that the theoretical valence of the (6x6) Cu supercell can be adjusted by the substituted phenyl groups [34,35] (Fig. 1a-b, Supplementary Figs.2 to 9 and Table 2). To gain understanding, we also analyzed the consequences of functionalization for the surface Cu atoms adjacent to the grafting site. Our results show that the nature of the substituents plays a crucial role in modulating the electron density of copper and the oxidation state of the surrounding atoms, ultimately influencing the catalytic activity of Cu-based systems (Fig.1c, Supplementary Figs.10 to 14 and Tables 3 to 5). We also note that our investigations point out to the formation of new interfaces with different valence states after functionalization with aryl diazonium salts, which originate from the orientation of the molecule on the Cu surface (Fig.1c). Such interfaces are analogous to the previously described Cu_2O/Cu catalyst proposed by Goddard group[15].

To clarify how the functional group affect the oxidation state of the Cu atoms and regulate the CO_2 reduction, we calculated the adsorption energy of CO_2 with explicit water molecules. We selected differently specific Cu sites on Cu-NN system with different theoretical valence: -0.018, -0.022, +0.029 and +0.105 for Cu99, Cu105, Cu66 and Cu60, respectively (Fig. 1d, Supplementary Figs.10 and 15, and Table 6). We found that the CO_2 adsorption energy gradually increased with the oxidation state when getting closer to the grafting sites. Among the examined Cu sites, Cu60, located closest to the functional groups, exhibited the highest theoretical valence (+0.105) and the lowest CO_2 adsorption energy (-0.468 eV). Conversely, the farther Cu site (Cu99) demonstrated the highest CO_2 adsorption energy. Our investigations point out that the CO_2 activation and its subsequent electrochemical reduction are likely to occur on the Cu sites in the vicinity of the functional groups, namely Cu60, Cu57 and Cu63, rather than on the outermost Cu99 atom of the Cu-NN catalyst or the directly grafted copper atoms, thanks to more stable adsorption. We calculated the adsorption energy of CO for the different Cu-X systems (See Methods section for details) and found that Cu-NN exhibits the

lowest adsorption energy compared to the other functionalized Cu as well as pristine Cu **(**Supplementary Fig.16 and Table 7). Our calculations also indicate a reduced energy barrier of CO dimerization on Cu-NN catalyst than pristine Cu and the CO dimerization step typically occur on Cu60, Cu66, Cu63 and Cu57 sites (Fig. 1e, Supplementary Figs.17 to 21 and Table 8). Collectively, our results demonstrate that introducing various electron-withdrawing aryl diazonium groups enables the modulation of the oxidation state (theoretical valence) of Cu. This modulation favors the CO_2 reduction and *CO dimerization into multi-carbon products by improving the adsorption energy of CO_2 and CO on specific sites near these functional groups. We finally evaluated the free energy of hydrogen adsorption (ΔG_{H^*}) on both pristine Cu and Cu-NN. Our results revealed that ΔG_{H^*} on Cu-NN is larger than for Cu indicating that aryl functionalization not only promotes the carbon-carbon coupling but also suppresses the competitive evolution of hydrogen (Supplementary Fig. 22 and Table 9). Overall, our investigations predict that functionalization with electron withdrawing groups favor the adsorption of CO_2 and CO and the reaction preferentially takes on the Cu atoms located near the grafting sites of the aryl diazonium salts.

Ethylene and ethanol are generally considered to share the same initial reaction pathway, starting from *COCOH but branching off from the *CH_2COH intermediate [36]. To get insight into the ethylene *vs.* ethanol selectivity, we explored the role of the oxidation state of $Cu^{\delta+}$ on the free energy of the successive intermediates along with the ethylene (*O+C_2H_4(g)) and ethanol (*C_2H_4O) pathways (Supplementary Figs.23 to 25). The calculations were systematically performed on pristine and $N(C_2H_{5)2}$, OCH_3, N, NN, NNN, Br and NO_2 functionalized Cu. Our results reveal a lower free energy for *O+C_2H_4(g) (ethylene pathway) than for *C_2H_4O (ethanol pathway) on Cu-NN. These findings indicate that rational functionalization with substituted aryl groups favors the formation of the *O+C_2H_4(g) intermediate by breaking the C-O bond instead of the direct hydrogenation of the C-H bond to form *CH_2CH_2OH (Fig.1f, Supplementary Fig.26 and Table 10). Of all functionalized Cu catalysts, Cu-NN displayed the lowest free energy of -1.63 eV towards ethylene, suggesting a

large selectivity for ethylene (Fig.1f). We also explored the influence of the electric field on the ethylene selectivity and found that the determining step to produce ethanol is independent on the electric field, while the energy associated to the ethylene formation rapidly decreases and reaction becomes exothermic under negative electric field values as the bias potential is increased[19,37-41] (Supplementary Fig. 27 and Table 11). To exclude any potential influence of the nature of the Cu facet on CO_2RR performance of Cu-X catalysts, we carried out DFT calculations on Cu (100) and Cu (111). We first calculated the theoretical valence of Cu (100) after functionalization and found that the valence of Cu (100)-X catalysts matches with the result from Cu (111)-X catalysts, suggesting that the influence of aryl diazonium groups on the theoretical valence of Cu is independent of the Cu facets (Supplementary Figs. 28 to 30 and Table 12). We then assessed the energy barrier of *CO dimerization as well as the energy of hydrogen adsorption on pristine Cu and all Cu-X catalysts (See Methods section for details). Our results demonstrate that the energy barrier for the *CO dimerization is lower on functionalized Cu (100) compared to that functionalized Cu (111) (Supplementary Figs. 31 to 36, and Table 13). This suggests that the Cu (100) facet has a higher activity towards the formation of multi-carbon products than Cu (111) facet, in agreement with the literature. These predictions are further corroborated by our experimental results on single crystals of Cu (111) and Cu (100), as well as the NN-functionalized Cu (111) and Cu (100) (Supplementary Fig. 37). We also found a higher free energy of hydrogen adsorption on all Cu (100)-X catalysts compared to bare Cu (100) indicating that the aryl groups on Cu (100) lower the HER activity of Cu (Supplementary Figs. 38 and 39, and Table 14).

Catalyst synthesis and characterization

In light of our numerical simulations, we sought to fabricate a series of copper catalysts *via* electrodeposition on a gas diffusion layer (GDL). The Cu catalysts were subsequently modified with aryl diazonium salts and labeled hereafter Cu-X where X represents the grafted aryl groups (Fig. 1a). The reactivity of aryl diazonium salts on copper follows two mechanisms: a direct attachment of the phenyl groups or the formation of new azo groups[26,42-45] (Supplementary Figs.

2 and 3). Based on our XPS analyses, we confirmed that the grafting mechanism involves the formation of azo bonds as evidenced by the presence of the signal at 400 eV. Signals from the N=N bonds were detected on all functionalized copper catalysts, including Cu-Br and Cu-OCH_3, with an estimated 3:2 molar ratio of Br/OCH_3 to azo (Supplementary Fig. 40 and Supplementary Table 15). The morphology and crystal structure of functionalized Cu catalyst do not substantially change after the modification with diazonium salts, suggesting functionalization does not induce amorphization of the Cu surface (Figs. 2a, b and Supplementary Figs. 41 to 43). In particular, high-resolution electron microcopy analyses showed the presence of a continuously functionalized layer at the surface of the catalysts with a thickness of about 5-8 nm (Figs. 2a, b and Supplementary Fig.44a). In addition, based on our EELS analyses (Fig. 2b and Supplementary Fig. 44b), we confirmed the presence of C and N in the functionalized layer, which highlights the successful grafting of diazonium molecules at the surface of the Cu catalyst. To further improve the gas and ion transport to the active sites in the MEA cell, a perfluorinated sulfonic acid (PFSA) ionomer was spray-coated on the catalyst (Supplementary Fig. 45). The use of ionomers has been recently introduced to promote gas, water, and ion transport due to their hydrophobic and hydrophilic functionalities and ion transport domains, respectively[7,46-48]. The presence of the PFSA ionomer was further confirmed by its characteristic Raman signatures at 733,1005 and 1130 cm^{-1}, which are associated with the -CF_2, C-C, and -SO_3 vibrations modes, respectively[7] (Supplementary Fig. 46)[7]. Energy-dispersive X-ray spectroscopy (EDS) elemental mapping further supports the uniform distribution of ionomer on the surface of Cu-NN catalyst (Supplementary Fig. 47).

To elucidate the relationship between the molecular doping properties of the aryl groups and the behavior of the functionalized catalysts properties, we systematically evaluated the CO_2RR properties in a zero-gap MEA cell using a 0.5 M $KHCO_3$ anolyte and 10 sccm of CO_2 as feed for the cathode. Compared to pristine (*i.e.* non-functionalized) Cu, all the Cu-X electrodes exhibited improved Faradaic efficiency for ethylene (Fig. 2c and Supplementary Fig. 48 and Supplementary Table16). We found a volcano relationship between the FE of C_2H_4 (FE_{C2H4})

and the applied potential and the Cu-NN catalyst exhibits the highest FE_{C2H4} at 83% for a full cell potential of -3.55 V. To explore the influence of the NN thickness on CO_2RR performance, we assessed the properties of Cu-NN electrodes having different thickness of aryl diazonium (See "Influence of the diazonium thickness" section in the Supporting Materials and Supplementary Fig.49). Our results reveal that thin and uniform coating enhances the formation of ethylene, while larger thickness results in performance degradation due to limited diffusion of CO_2 to the active sites of Cu and non-uniform coating.

To investigate the correlation between the FE_{C2H4} and the oxidation state of different diazonium salts functionalized copper, we plotted the experimental FE_{C2H4} against the valence of the Cu sites predicted by our DFT calculations. We found a volcano trend that peaks at 83% at an average Cu valence of + 0.26, corresponding to the Cu-NN electrodes (Fig. 2d). We also observed a strong correlation between the ratio of FE_{C2H4} to FE_{C2H5OH} as a function of the calculated theoretical valence, confirming the influence of the valence on the selectivity of ethylene over ethanol (Supplementary Fig. 50). A FE_{C2H4}-to-FE_{C2H5OH} ratio as high as 38 is obtained on Cu-NN and agrees with our DFT predictions that $Cu^{\delta+}$ triggers the formation of ethylene rather than ethanol (Supplementary Figs. 50a and b). The performance of both Cu-NN and pristine Cu were further increased in the presence of PFSA ionomer, and the Faradaic efficiency for ethylene reached 89±3% and 48±4% at a specific current density of C_2H_4 of 536 mA cm^{-2} and 269 mA cm^{-2}, respectively (Supplementary Figs. 51 and 52). To gauge the stability of our functionalization strategy, we operated the MEA cell at a full cell voltage of -3.55 V for 120 h using Cu-NN as CO_2RR catalyst. We obtained a stable current at approximately 1 A with an average FE for C_2H_4 of 79% corresponding to a retention of 95% in a neutral medium (Fig. 2e). Furthermore, to examine the stability of functional group (NN) on copper, we also characterized the surface of Cu-NN catalyst after 24 hours reaction (hereafter aCu-NN) by using Raman and high-resolution electron microcopy (HRTEM). The Raman signatures of the functional groups are clearly detected, while the HRTEM images of aCu-NN show no significant changes in the morphology and surface coating, highlighting the stability of the

functionalized catalyst (Supplementary Fig. 53).

Next, we sought to evaluate the selectivity, the energy efficiency (EE) and the electrical power consumption (EPC) for the production of C_2H_4 in a MEA cell. Compared to other literature benchmarks[6,7,9,49-54], both Cu-NN and Cu-NN/ionomer catalysts demonstrated improved selectivity towards ethylene and higher energy efficiency at the same specific current density of ~200 mA cm^{-2} (Figs. 2f and g, Supplementary Table 17). Remarkably, the EPC for the formation of ethylene on Cu-NN is 10% lower compared to the best-reported catalyst tested in the same device configuration, suggesting a lower threshold to meet industrial requirements (Fig. 2h, Supplementary Table 17). To confirm the improvement of the intrinsic CO_2RR properties after aryl functionalization, we finally estimated the electrochemically active surface area (ECSA) of pristine Cu, Cu-NN and Cu-NN/ionomer catalysts by using the Pb underpotential deposition method (Pb_{UPD}) (Supplementary Fig. 54a and Supplementary Table 18). The ECSA-normalized partial current densities for C_2H_4 measured in the MEA cell are 96 mA cm^{-2} and 212 mA cm^{-2} for Cu-NN and Cu-NN/ionomer, which are ~2 and ~4.5 times higher than in the case of pristine Cu, respectively (Supplementary Fig. 54b). To rule out any preferential attachment of the aryl groups on the Cu surfaces, we examined the functionalization on Cu(111) and Cu(100) single crystals, and compared their respective surface coverage by assessing their electrochemically active surface areas. Our results revealed that the surface coverage of NN on Cu(111) and Cu(100) single crystals are 20.8% and 22.0%, with estimated ECSAs of 1.20 cm^2, 1.27 cm^2, 0.95 cm^2 and 0.99 cm^2 per geometrical cm^2 of Cu(111), Cu(100), Cu(111)-NN and Cu(100)-NN catalysts, respectively. These values are close to the surface coverage obtained for electrodeposited Cu-NN: 18.7%, suggesting that there is no preferential attachment of the aryl groups on Cu (Supplementary Fig. 55 and Supplementary Table 19).

***Ex-situ* and *operando* investigations**

To investigate the impact of the aryl functionalization on the oxidation states of copper, we first performed ex-situ X-ray photoelectron spectroscopy (XPS) on the different Cu-X catalysts. When examining the Cu2*p* spectra, the absence of satellites confirms that there is no Cu^{2+}

(Supplementary Fig. 56). As it is difficult to distinguish the Cu^+ from the Cu from the Cu2*p* spectra, we examined the LMM Auger signals from freshly prepared Cu-X samples to precisely evaluate the oxidation state of copper[55]. According to the deconvolution of the Auger LMM spectra, we found that the Cu-NO_2 surface has the largest ratio of Cu^+ to Cu and the average oxidation state is estimated to be +0.75, while Cu-$N(C_2H_5)_2$ has the smallest oxidation state at δ=+0.13 (Supplementary Table 20).

We then carried out X-ray absorption near-edge spectroscopy (XANES) on the Cu-X catalysts to assess the Cu oxidation state. Before testing, a negative potential (-0.7 to -2.0 V versus reversible hydrogen electrode (RHE), 60 mV s^{-1}, 3 cycles) was applied on Cu-X samples to exclude oxygen-containing species. The absorption edges of all Cu-X samples reside between those of pristine copper (Cu^0) and Cu_2O used as a reference (Cu^+) (Fig. 3b and Supplementary Fig. 57). To obtain a direct comparison of the oxidation state of copper in the different Cu-X catalysts, we plotted the copper oxidation state as a function of energy shift of the Cu K-edge (Fig. 3b inset). From the linear fit of the positions for Cu^0 and Cu^+ (Cu_2O), we determined the average oxidation state of the Cu-X catalysts to range between +0.13 to +0.75 as a function of the electron-withdrawing ability of substituted phenyl groups. Cu-NN exhibits an oxidation state of δ=+0.27, which is remarkably close to the calculated theoretical valence of copper (δ=+0.260) (Supplementary Table 21). To further explore the stability of $Cu^{\delta+}$ species on Cu-NN, we performed o*perando* X-ray absorption spectroscopy (XAS) at applied potentials of -0.93 V, -0.88 V, and -0.83 V *vs.* RHE (Supplementary Figs. 58 and 59). Close examination of the XAS spectra suggests a minimal perturbation of the oxidation state of Cu during the CO_2RR. We determined the average oxidation states of copper in Cu-NN to be +0.25, +0.23, and +0.19 at -0.93 V, -0.88 V, and -0.83 V *vs.* RHE, respectively close to that obtained from our *ex-situ* analyzes (Supplementary Tables 22 and 23).

To increase our understanding of the role of different functional groups in promoting the formation of ethylene, we studied the adsorbed CO on the surface of the Cu-X catalysts using operando Raman spectroscopy (Supplementary Figs. 60 to 62). Two different types of defect

sites – isolated defect-like sites and step-edge sites have previously been identified on copper[56] and have been linked to the *CO dimerization associated with the formation of C_{2+} products[6,56-58]. According to previous operando measurements from the literature on well-defined system, *CO-bound on step-edge sites is usually assigned to the dynamic LFB-*CO and is related to C-C coupling[56], whereas the presence of the relative static HFB-*CO peak at ≈2080 cm^{-1} is ascribed to adsorbed *CO on isolated defect-like sites and more related to gaseous CO production[56]. Qualitatively, we also observed a linear correlation between the adsorption energy of CO and the CO Raman signals (Supplementary Figs.62 and 63). We then examined the high-frequency band (HFB-*CO) and the low-frequency band (LFB-*CO) of CO at ~2087 cm^{-1} and ~2060 cm^{-1}, respectively[57,59,60] (Fig. 3c). These bound CO configurations were identified and quantified using *operando* Raman spectroscopy for the different Cu–X catalysts at a fixed potential of -0.88 V *vs.* RHE (Supplementary Fig. 51 and Supplementary Table 24)[6,57,61,62]. The HFB-*CO-to-LFB-*CO ratio on all Cu–X catalysts are larger compared with bare Cu, and presents a clear linear correlation with the average oxidation state of copper (Fig. 3c). We attribute the change in the ratio of HFB-*CO-to-LFB-*CO on Cu–X catalysts to the different adsorption energy of CO by the tailored oxidation state of surface copper sites through different substituted aryl groups, as revealed by our calculations of the adsorption energy of CO (Supplementary Fig. 16 and Supplementary Table 7). Our investigations indicate that the average oxidation state of copper should be neither too high nor too low. We found a volcano-shaped relationship between the ethylene selectivity and the HFB-*CO-to-LFB-*CO ratio on the Cu–X surfaces, which highlights the importance of the balance between step-edge sites and isolated defect-like sites on Cu for the adsorption of CO and the promotion of the C-C coupling. Cu-NN seats near to the top of the volcano, pointing out to a possible stabilization of HFB-*CO relative to LFB-*CO on mildly oxidized $Cu^{\delta+}$ ($0<\delta<1$).

We compared the *operando* Raman spectra of Cu-NN and pristine Cu catalysts (Figs. 3d and e) for different potentials. The Raman heat map of the Cu-NN and pristine Cu revealed a clear enhancement of the signals from adsorbed CO in the case of Cu-NN, which qualitatively

indicates that larger amounts of CO intermediates are readily available for the further C-C coupling. We also found that Cu-NN displays strong HFB-*CO and LFB-*CO signals for potentials between -0.48 V and -0.7 V *vs.* RHE up to -0.88 V *vs.* RHE, while no signals can be detected from pristine Cu (Fig. 3e). This points out to a greater energy barrier to produce CO intermediates, thus limiting the formation of C_{2+} products. As the final evidence, we plotted the FE for CO and C_2H_4 as functions of the potential to visualize the intertwining between the Raman signatures of adsorbed CO and the selectivity for C_{2+} products (Figs. 3d and e). To exclude any contribution from the interactions between CO_2 and the substituted aryl groups on Cu, we performed CO_2-temperature programmed desorption (TPD) on the functionalized Cu catalysts (See "TPD analyses" section in the Supporting Materials and Supplementary Fig.64). The results showed no significant correlation between the interaction of the aryl groups with CO_2 and the catalytic activity, indicating that the valence state of copper is the main factor in promoting CO_2RR. Moreover, the influences of total current density on the oxidation state of copper and the water contact angle of functionalized copper electrodes on CO_2RR performance were also examined. No obvious correlation was observed (Supplementary Figs.65 and 66), which further highlights the dominant role of electro-withdrawing functional groups in controlling the valence of copper and enhancing the catalytic performance.

Direct *vs.* cascade flow processes for the formation of C_2H_4

The electrical power consumption is one the primary obstacle for the development of the CO_2RR. Although progress has been made in the direct electroreduction of CO_2 to C_2H_4 in MEA cells with appreciable selectivity and high current density, the requested full-cell potential makes the production cost of ethylene uncompetitive compared to industrial-grade ethylene obtained from steam cracking of oil or natural gas. In addition, the formation of carbonate in the MEA reactor combined to the strongly alkaline conditions leads to poor performance stability and low CO_2 single-pass conversion rate due to the flow of hydroxide ions from anode that reacts with gas CO_2. Technical-economic analyses have suggested that a high specifically

current density (>150 mA cm^{-2}), and low operating full-cell potential (< 3 V) are the necessary requirements to compete with the traditional ethylene production process[50]. CO can advantageously replace CO_2 to produce multi-carbon species *via* the CO reduction reaction (CORR). The CORR is compatible with alkaline electrolytes at the anode to prevent the competitive hydrogen evolution reaction without significant carbonate formation that typically plagues the conversion of CO_2[63]. It is also anticipated that the CORR can improve the charge transfer kinetics and the selectivity towards ethylene, while decreasing the energy footprint of the system[11,12,64]. The realization of cascade flow processes has recently been explored to convert CO_2 to CO and then use CO to produce C_{2+} products[65,66].

In light of this, we sought to develop an integrated flow electrochemical system for the energy-efficient conversion of CO_2 to C_2H_4 by coupling two MEA cells using Cu-NN as CORR catalyst. Considering the high market price of iridium (at ~ 6k$ per once, +375% since Nov. 2020), we thought to replace expensive IrO_x with NiFe based layered double hydroxide (NiFe LDH) as anode catalyst[67]. We confirmed that NiFe LDH shows a lower overpotential than IrO_x toward the OER in 1 M KOH (Supplementary Fig. 67). We then estimated the CO_2-to-CO performance using electrodeposited Ag and NiFe based layered double hydroxide (NiFe LDH) as cathode and anode, respectively. We achieved a 94% FE for CO at the full-cell potential of -3.55 V and a specific current density for CO of 119 mA cm^{-2} for an inlet flow rate of 10 sccm of CO_2 (Supplementary Fig. 68, and Supplementary Table 25). We evaluated the single-pass conversion efficiency (SPCE) to be ~31% at -3.55 V. To achieve an optimal CO feed of ~4.6 sccm, we set the full-cell voltage of the first MEA cell to -3.8 V corresponding to a FE and specific current density for CO of ~84% and 166 mA cm^{-2}, respectively. The outlet gas from the Ag-based MEA was purified using a CO_2 capture solution containing 30% ethanolamine and then introduced into the second MEA cell for the CO-to-C_2H_4 conversion. We tested the CO-to-C_2H_4 conversion system using pristine Cu, Cu-NN, and Cu-NN/ionomer as cathode, and IrO_x as anode catalysts. The FE for C_2H_4 on Cu-NN reached a record-high values for the CORR at ~86.0% and a full-potential of -2.5 V. Cu-NN clearly outperforms Cu and Cu-NN/ionomer

with FE_{C2H4} of ~67.4% and ~72. 1%, respectively (Supplementary Fig. 69 and Supplementary Table 26).

The operating cell voltage (E_{Cell}) for the CO_2RR is known to be responsible for a significant electrical consumption and the oxidation evolution reaction (OER) at the anode brings a high energy penalty to the process[5]. By operating the cascade MEA cells with NiFe LDH and Cu-NN as anode and cathode catalysts, we achieved an optimal E_{Cell} of -2.3 V for maximizing the production of ethylene with a FE_{C2H4} of ~86% (Fig. 4a and Supplementary Fig. 70 and Supplementary Table 27). We determined a stable full-cell energy efficiency of 39.6% and a 12.3% CO_2-to-C_2H_4 cascade single pass conversion efficiency for the cascade flow process with a specific current density of 154 mA cm^{-2}. For comparison, Cu-NN/ionomer and pristine Cu catalysts exhibit EEs of 30.5% and 27.4% and CO_2-to-C_2H_4 cascade conversion rates of 12.9% and ~6.0% at -2.3 V, respectively (Figs. 4b and c, Supplementary Fig. 71 and Table 28). The formation rates of ethylene on Cu-NN/ionomer increased by 191% compared to pristine Cu electrodes. We estimated an EPC value of only 25.6 kWh Nm^{-3} for the Cu-NN+NiFe LDH system – lower than for Cu-NN/ionomer and Cu (Fig.4b and Supplementary Table 29). Remarkably, the cascade system maintained a 10.7 % CO_2-to-C_2H_4 conversion rate at an average specific current density of 140 mA cm^{-2} for 100 h (Fig.4d and Supplementary Table 29). We finally compared the performance of the Cu-NN and Cu-NN/ionomer catalysts with previous literature benchmarks[6,7,49,50,52,65,66,68-70] and found that Cu-NN display greater energy efficiency and lower EPC for both the direct and the cascade flow processes (Figs. 5a and b).

To validate the proposed concept, we functionalized commercial Cu particles (cCu) (Supplementary Figs. 72 to 74) and examined their performance in MEA electrolyzers. Our results showed that even on the not optimized Cu catalysts, the Faradaic efficiency of ethylene on cCu-NN electrode can reach 42% at – 3.7 V compared to ≈ 20% for the pristine Cu particles. Importantly the energy efficiency and the electrical power consumption were improved by 31 % and 23.5% upon functionalization (Supplementary Table 30). Functionalization of the Ag electrode with NN leads to a slight decrease in the FE_{CO} (Supplementary Figs. 73 and 75), but

a higher specific current density of CO than pristine Ag (Supplementary Figs. 75c) indicating improved kinetics. Furthermore, we evaluated the role of the counter ion of the aryl diazonium salts on the CO_2RR properties and found that the nature of the anion has a negligible effect on the CO_2RR properties (Section "Influence for the anion on the CO_2RR activity" section in the Supporting Information, Supplementary Fig. 76)

To assess the economic viability of electro-reduction of CO_2 to C_2H_4 on Cu, Cu-NN, and Cu-NN/ionomer, we carried out techno-economic analyses by comparing the direct conversion route (CO_2-to-C_2H_4 in a single reactor) with the two steps cascade systems (CO_2-to-CO, and CO-to-C_2H_4 in cascade system). We considered a single MEA cell to convert CO_2 to C_2H_4 using a neutral 0.5 M $KHCO_3$ anolyte, while 0.1 M $KHCO_3$ and 1 M KOH were used as anolytes in the first and the second MEA cells for the CO_2-to-CO, and CO-to-C_2H_4 reactions (See Note S1 in the Supplementary Information for details). We determined the OPEX of the direct and the cascade flow processes for the production of 1 ton of C_2H_4 with/without the use of ionomer. In our calculations, we assumed a catalyst lifetime of one year (8,760 hours) and a total electrode surface of 100 m^2. Figs. 5c and d show the cost distribution for the different parameters, without considering the CO_2 loss due to carbonate formation and membrane crossover as well as the downstream separation costs. We note that the installation costs and the balance of plant are part of the capitalization expenditure (CAPEX) and are not included in our calculations (See Note S2 in the Supplementary Information file). Among the four different MEA configurations, we found that direct conversion of CO_2 to ethylene using Cu-NN and ionomer is the closest to profitability. Importantly the cost of ethylene production decreases from 12,600 \$ ton^{-1} to 4,500 \$ ton^{-1} using pristine Cu and Cu-NN/ionomer electrodes, respectively, which corresponds to a 64% reduction. The analysis of the cost breakdown highlights that, in absence of ionomer, the main expense items for the direct production of the C_2H_4 from CO_2 are the anode catalyst and the membranes for a total of 57.4% of the production cost. The use of ionomer lowers the cost (per ton of C_2H_4) of most parameters due to the improvement of the yield rate of the process and the EPC accounts for most of the expenses (32.6%) (Figs. 5c and d). Conversely, in the

cascade configuration, the cost of the anion-exchange membrane (AEM) represents the main expense for Cu-NN and Cu-NN/ionomer conditions at 47.1% and 39.4%, respectively (Figs. 5c and d). These findings point to the opportunity to rapidly improve the profitability of CO_2RR by decreasing the cost to electrolyte membranes (Supplementary Table 31). Overall, aryl functionalized $Cu^{+0.26}$ holds potential to lower the financial gap between the low carbon-footprint CO_2RR technology and the traditional ethylene production based on fossil resources.

Conclusions

This work presents a novel approach to orient the CO_2RR and the CORR towards the production of ethylene with record-high selectivity and formation rate. The origin of the high selectivity for C_{2+} products is attributed to the formation of stable $Cu^{\delta+}$ ($0<\delta<1$) as supported by our *operando* and *ex-situ* physical characterizations using XPS, XAS and Raman spectroscopy. We attributed the near-unity selectivity for C_2H_4 among the C_{2+} products to the lower energy associated with the formation of the $*CH_2CH$ intermediate on $Cu^{0.26+}$. When implemented in a neutral MEA cell, the Cu-NN catalyst achieved a FE for ethylene of 83 ± 2 % with a partial ethylene current density of 212± 3 mA cm^{-2}. The full-cell EE and the conversion efficiency for ethylene can be further increased to 39.6% and 12.3%, respectively, with a low record-low EPC of 25.6 kWh/Nm^3 by replacing CO_2 for CO in a cascade flow process. Our findings provide a route towards practical developments for the CO_2-to-C_2H_4 conversion reaction using valence engineering of the Cu sites.

Methods

Catalyst preparation. The Cu catalyst was electrodeposited at a constant current of -15 mA cm^{-2} for 300 s on an acid-treated gas diffusion layer (GDE, Sigracet 22BB, for characterizations) with CO_2 gas flow (60 sccm). The solution consisted of 0.1 M copper bromide (98%, Sigma-Aldrich), 0.2 M sodium tartrate dibasic dihydrate (purum pro analysis ≥ 98.0% non-aqueous

titration (NT), Sigma-Aldrich), and 1 M KOH. Ag electrodes were prepared by electrodeposition in a solution of 0.01 M $AgNO_3$, 0.6 M $(NH_4)_2SO_4$, and 0.04 M ethylenediamine at a current density of 10 mA cm^{-2} for 15 min. Nafion 117 and anion exchange membrane (Sustainion® X37-50), gas diffusion layer, and titanium mesh were obtained from the Fuel Cell Store. To prepare the Cu electrodes with commercial copper, 200 mg copper particles (the size of 2~3.5 μm, Sigma 7440-50-8) were firstly dissolved into the solution of 35.3 mg Nafion ionomer, 35.3 mg XC-2 ionomer (Carbon Dioxide) and 4 ml iso-propanol, as well as 4 ml deionized water. Then, the prepared ink was spray coated on a porous gas diffusion layer (Sigracet 22BB) with a loading amount of 1 mg/cm^2. All chemicals were used as received. All aqueous solutions were prepared using deionized water with a resistivity of 18.2 MΩ cm^{-1}.

Functionalized Electrodes preparation. The Cu electrodes were functionalized in Ar-saturated aqueous solution containing 3mM corresponding diazonium salt. The used aryl diazonium salts in the experiment are 2-Methyl-4-(2-methylphenylazo)benzenediazonium salt (NN, Fast Garnet GBC sulfate salt, Sigma-Aldrich), 4-Amino-4′-methoxydiphenylamine-diazonium chloride (N, Variamine blue B salt, Sigma-Aldrich), 2,5-Dimethoxy-4-([4-nitrophenyl]azo)benzenediazonium chloride hemi(zinc chloride) salt (NNN, Fast Black K Salt hemi(zinc chloride) salt, Sigma-Aldrich), 4-Methoxybenzenediazonium tetrafluoroborate (OCH_3, 98%, Sigma-Aldrich), 4-Bromobenzenediazonium tetrafluoroborate (Br, 96%, Sigma-Aldrich), 4-Nitrobenzenediazonium tetrafluoroborate (NO_2, 97%, Sigma-Aldrich) and 4-Diazo-*N*,*N*-diethylaniline fluoroborate($N(C_2H_5)_2$, abcr. Gute Chemie), 4-Aminodiphenylamine diazonium sulfate (Variamine Blue RT Salt, Sigma-Aldrich). All chemicals were used as received and all aqueous solutions were prepared by using deionized water with a resistivity of 18.2 MΩ cm^{-1}. The aryl diazonium salts were electrodeposited onto all electrodes (the electrodeposited Cu-GDL electrode, the spray-coated commercial Cu-GDL electrode and the electrodeposited Ag-GDL electrode) using a three-electrode setup with Cu-GDL electrode, Ag/AgCl (3.5 M KCl) and a Pt plate as working, reference and counter electrodes, respectively. A constant current of 0.70 mA cm^{-2} was applied for 100 s on the Cu-GDL electrode (~2.0 × 2.0

cm^2 for MEA) by using a potentiostat (VSP potentiostat from Bio-Logic Science Instruments). After electrodeposition, the electrode was rinsed with DI water, dried under Ar, and stored in glovebox for further use.

Ionomer deposition. Cu-NN electrodes were modified by spray-coating a PFSA solution. The PFSA solution were prepared by using 700 mg of ionomer (Nafion perfluorinated resin solution, product #527084-25 ml purchased from Sigma Aldrich) and 25 ml methanol (99.8%, anhydrous, Sigma Aldrich). The optimal loading with ionomer was achieved by tuning the spray-coating conditions in order to reach a desired loading of 1.75 mg cm^{-2}. Samples were dried for at least 24 h at room temperature in a vacuum chamber before operation.

Materials characterization. A field emission scanning electron microscope (TESCAN Mira3) was employed to observe the morphology of samples. Aberration-corrected high-resolution (scanning) TEM imaging (HR-(S)TEM), energy-dispersive X-ray spectroscopy (EDS) and spatially-resolved electron energy-loss spectroscopy (SR-EELS) were performed using a FEI Titan Cubed Themis microscope which was operated at 80 kV. The Themis is equipped with a double Cs aberration corrector, a monochromator, an X-FEG gun, a super EDS detector, and an Ultra High Resolution Energy Filter (Gatan Quantum ERS) which allows for working in Dual-EELS mode. HR-STEM imaging was performed by using high-angle annular dark-field (HAADF) and annular dark-field (ADF) detectors. SR-EELS spectra were acquired with the monochromator excited allowing an energy resolution of 1.1 eV with an energy dispersion of 0.4 eV/pixel. X-ray photoelectron spectroscopy (XPS) measurements were carried out on Thermo Electron ESCALAB 250 System using Al Kα X-ray radiation (1486.6 eV) for excitation. Raman measurements were conducted using a Renishaw in Via Raman microscope and an ×50 objective (Leica) equipped with a 633 nm laser. *Operando* Raman measurements were carried out using a modified liquid-electrolyte flow cell using a 20 s integration time and averaging 10 scans per region. The spectra were recorded and processed using the Renishaw

WiRE software (version 4.4). Ag/AgCl (3.5 M KCl) and a Pt plate were used as the reference and counter electrodes, respectively.

X-ray absorption spectroscopy (XAS). *Ex situ* X-ray absorption spectra at the copper K-edges and Operando X-ray absorption spectroscopy (XAS) measurements at the copper K-edges were collected at ALBA Synchrotron Radiation Facility (Barcelona, Spain) on beamline CLAESS and SOLEIL Synchrotron Radiation Facility (Saint-Aubin, France) on beamline SAMBA, respectively. Measurements were performed mainly in fluorescence mode, but transmission XAS data were also collected for comparison.

In SOLEIL Synchrotron Radiation Facility, the beamline is equipped with a sagittally Si (111) monochromator at the Cu K-edge for energy selection. The beam size was 1 × 0.5 mm. The signals were collected in fluorescence mode using a 13-channel Ge detector. The intensity of the incident radiation was measured with an ionization chamber (I_0) filled with an N_2 (500 mbar)/He (500 mbar) mixture. Two additional ionization chambers filled with 1700 mbar N_2 (in I_1 chamber) and an Ar (150 mbar)/N_2(850 mbar) mixture (in I_1 chamber) were used for measurements in transmission mode in the case of the reference samples.

In ALBA Synchrotron Radiation Facility, intensities of the incident radiation and transmitted radiation were measured with ionization chamber detectors I_0 and I_1 filled with pure N_2 (I_0 chamber) or 70:30 N_2 and Kr mixture (I_1 chamber). Fluorescence data were collected using energy selective 6-channel Si drift detector. Si (111) monochromator was used for energy selection. XAS data for Cu foil, Cu_2O, and CuO reference samples were also collected for comparison and data alignment.

For the XAS studies, Cu was firstly electrodeposited on gas diffusion layer (GDL, Sigracet 22 BB, Fuel Cell Store) used as gas diffusion electrode (GDE) and then functional solutions were modified on the catalyst side, while the other side of the GDL was covered with polyamide tape. The GDL was then taped on a graphite foil and subsequently, the electrode was mounted in our home-built single compartment cell, where the samples on graphite foil acted as a working electrode. Pt mesh and Ag/AgCl were used as counter and reference electrodes,

respectively. The applied potential was controlled with BioLogic potentiostat. As for the electrolyte, we used an aqueous solution of CO_2-saturated 0.5 M $KHCO_3$ that was continuously circulated through the cell using a peristaltic pump. The electrolyte was continuously purged with CO_2 with a flow rate of 20 ml/min. All measurements were performed at constant potentials of -0.98 V, -0.93 V, -0.88 V and -0.83 V vs. RHE. Time-resolved spectra under CO_2RR conditions were acquired every 12-15 min until no further changes were observed.

Data alignment and normalization of the X-ray absorption near edge structure (XANES) spectra were carried out using the Athena software. Fitting of the Cu K-edge extended X-ray absorption fine structure (EXAFS) spectra $\chi(k)k^2$ of the catalysts was carried out in R-space in the range from R_{min} = 1.0 Å up to R_{max} = 2.7 Å. The Fourier transforms were carried out in the k-range from 3.0 $Å^{-1}$ to 10.0 $Å^{-1}$ with a k-weighting of 1, 2 and 3. Fitting parameters were the coordination numbers N, interatomic distances R, disorder factors σ^2 for Cu-O and Cu-Cu paths, as well as the corrections to the photoelectron reference energies ΔE_0. Amplitude reduction factor S_0^2 = 0.94 was determined from the fitting of EXAFS spectra for Cu foil.

Computational details.

All density functional theory calculations presented in this paper are performed by using the Vienna Ab-initio simulation software package (VASP)[71] with the projected- augmented-wave (PAW)[72] and the Perdew-Burke-Ernzerhof (PBE) exchange correlation functional methods[73]. The energy cutoff was set to 400 eV and the Brillouin zone was sampled by a Gamma 1×1×1 K-point grid for structural optimization, while a 3×3×1 K-point grid was used for electronic state analysis. During structural optimization, the position of all the atoms except the bottom layer were relaxed and convergence criterion for the maximum force and energy on each atom was set to -0.05 eV/A˚ and 10^{-4} eV, respectively. In order to accurately describe the weak interactions, the dispersion-corrected DFT-D3 method[74] was employed to consider the van der Waals (vdW) interaction. For our calculations, we first designed a Cu (111) supercell (4 metal atoms in x direction, 4 metal atoms in y direction and 3 layers in z direction) with different aryl

diazonium salts after considering both experimental results and the steric-hindrance effects from the functional groups on the Cu surface. To accurately evaluate the valence of copper after functionalization, we calculated the valence of copper without solvent, as the strong electron-withdrawing ability of the oxygen atom from water molecules would withdraw some electrons from copper. Next, we calculated the valence of copper with explicit water to better replicate the experimental environment of the reaction. Periodic boundary conditions were used in all directions and 20 Å of vacuum layer was used in the z direction to separate the slabs. The two uppermost slab layers and the adsorbates were allowed to relax.

Theoretical valence analysis The theoretical valence of the copper atoms was calculated using the Bader Charge Analysis script written by Henkelman and co-workers[75]. The theoretical valence of the whole Cu super cell was evaluated according to the number of net charge obtained by the grafted aryl diazonium salts. We calculated the net charge (NCharge) of different grafted aryl diazonium groups by getting a sum of net charge of all atoms on aryl diazonium group. For each atom, the net charge (NCharge) is calculated by using the calculated formal Bader charge of the atom (NBader) to subtract the outermost electron number (NValence) of the related atom (1, 4, 5, 6 and 7 for H, C, N, O and Br, respectively), as follows [6,15,19]

$$NCharge = NBader - NValence \quad (1)$$

For example, taking one nitrogen atom on NN, the net charge is 5.536-5=0.536, indicating that the nitrogen atom receives 0.536 electron. After functionalizing with different aryl diazonium salts, the valences of bonded Cu systems – calculated with explicit water – are characterized by positive charges with the values of +0.149 e, +0.206 e, +0.219 e, +0.260 e, +0.497 e, +0.630 e and +0.787 e for $N(C_2H_5)_2$, OCH_3, N, NN, NNN, Br and NO_2 functional groups, respectively. This compares with the values of +0.173 e, +0.285 e, +0.307 e, +0.341 e, +0.590 e, +0.728 e and +0.843 e for $N(C_2H_5)_2$, OCH_3, N, NN, NNN, Br and NO_2 functional groups calculated in absence of solvent. The valences of nearby Cu atoms are also characterized by the same methods.

Calculations of the CO_2/CO adsorption energy over functionalized Cu. The adsorption energy of CO_2/CO molecules over a Cu surface in the presence and absence of functional groups was calculated using Equations (2a, b):

$$E_{ad-CO2} = E_{(CO2,slab)} - E_{(slab)} - E_{(CO2,gas)} \qquad (2a)$$

$$E_{ad-CO} = E_{(CO,slab)} - E_{(slab)} - E_{(CO,gas)} \qquad (2b)$$

where $E_{(CO2,\ slab)}$ and $E_{(CO,\ slab)}$ represent the total energy for CO_2 and CO molecules over the Cu slab; E_{slab} is the total energy of the bare slab. $E_{(CO2,\ gas)}$ and $E_{(CO,\ gas)}$ are the carbon dioxide and carbon monoxide gas phase energy. In our calculations, the more negative value of the adsorption energy represents a stronger binding strength of the CO_2/CO molecule.

Relationship between the Cu valence and the CO_2 adsorption energy in Cu-NN system. To understand how the functional groups affect the valence of Cu atoms and the related CO_2 adsorption energy near the grafting site, we chose NN-functionalized Cu as a model catalyst. For the calculations, we used a larger (3x3) supercell of Cu (111), including 6 metal atoms in the x direction, 6 metal atoms in the y direction and 3 layers in the z direction. A total of ten models were constructed varying the distance between NN-bonded Cu atom (i.e. the grafting site) and the CO_2 molecule from ~ 3.9 to 9.6 Å.

Calculations of the energy barrier associated with CO dimerization over functionalized Cu. To investigate the OC-CO coupling energy barriers on different Cu surfaces, a climbing image nudged elastic band (CI-NEB) method[76] was used to explore the transition state, followed by the dimer method to converge the saddle point within 0.05 eV/Å. Four windows were inserted between the initial state (IS) and the final state (FS) to identify the transition state (TS) when calculating the OC-CO coupling process on both pure Cu and Cu-NN. For all the intermediates and the transition states, five water molecules are added near the surface to take into account the effect of solvation [6,15,19,37,76,77]. Goodpaster, Norskov, Goddard, Neurock, and others have widely explored and simulated electric fields and charging effects by different methods[15,37,39,40,64,77]. We applied the Neugebauer and Scheffler method to include an applied electric field (-0.8 to 0.8 V/Å)[41] parallel to the vacuum layer in order to examine how the applied

electric field influences the selectivity of ethylene and ethanol in the presence of aryl diazonium salt (NN). the Gibbs free energy can be calculated using Equation (3), initially proposed by Nørskov et al[78],

$$\Delta G = \Delta E_{DFT} + \Delta E_{ZPE} - T\Delta S \qquad (3)$$

where T = 298.15 K, ΔE, ΔE_{ZPE} and ΔS are the total electron energy difference, zero-point energy difference and entropy change, respectively. The entropy change being small, its effect can be ignored.

Calculations based on Cu (100) models

We designed a series of Cu (100) supercells (6 metal atoms in x direction, 6 metal atoms in y direction and 3 layers in z direction) with different aryl diazonium salts after considering both experimental results and the steric-hindrance effects from the functional groups on the Cu surface. We calculated the theoretical valence of Cu, the energy barrier of *CO dimerization, and the free energy of hydrogen evolution reaction on all Cu (100)-X supercells with the consideration of solvent by using the same method as in calculating Cu (111)-X supercells.

Electrochemical in H-Cell and MEA configuration. All electrochemical measurements were carried out at ambient temperature and pressure using a VSP electrochemical station from BioLogic Science Instruments equipped with a 5 A booster and FRA32 module. The cell voltages reported in all figures were recorded without iR correction. All the potentials in the H-cell were converted to values with respect to the RHE potential using:

$$E_{RHE}=E_{Ag/AgCl}+0.197\ V+0.0591\times pH \qquad (4)$$

In the H-cell configuration, Ag/AgCl (3.5 M KCl) and a Pt plate were used as reference and counter electrodes respectively. The electrolyte consisted in a 0.5 M KOH solution (99.9%, Sigma Aldrich), which was saturated with alternatively CO_2 (≥99.998, Linde) or Ar (5.0, Linde). Prior to any experiment, the anolyte and catholyte solutions were saturated by bubbling CO_2 or Ar for at least 20 min.

The MEA electrolyzer (Dioxide Materials) was composed of the Cu cathode, a Ti-IrO_x mesh anode and an anion exchange membrane (AEM, Sustainion® X37-50, Fuel cell store). The

anode and cathode flow fields are made of titanium and stainless steel with geometric active areas of 4 cm^2 respectively. The anode was prepared by depositing IrO_x on a titanium support (0.002'' thickness, Fuel Cell Store) by a dip coating followed by thermal annealing. Briefly, the titanium mesh was firstly degreased with acetone and DI water, then etched in a 6 M HCl (Reagent Grade, Bioshop) solution heated to 80 ^oC to 90 ^oC for 45 min before dip coating. The solution used for dip coating consisted of 30 mg of $IrCl_3.xH_2O$ (Alfa Aesar) dissolved in 10 mL of an iso-propanol solution with 10% concentrated HCl. The etched titanium mesh was dipped into the $IrCl_3$ solution, dried in an oven at 100 ^oC for 10 min before calcination in air at 500 ^oC for 10 min. The dipping and calcination process was repeated until a suitable loading was achieved (2 mg cm^{-2})[70].

The AEM was firstly placed between the anode and cathode flow fields and then assembled together. The flow fields were mainly responsible for the effective supply in aqueous anolyte solution and humidified CO_2 over the respective surfaces of anode and cathode electrodes. The anode and cathode gaskets were placed between the flow fields and the respective electrodes to ensure proper sealing. An anion exchange membrane (Sustainion® X37-50) (Dioxide Materials) was activated in 1 M aqueous KOH solution for at least 24 hours, washed with deionized water and used as the anion-exchange membrane (AEM). A 0.5 M $KHCO_3$ anolyte solution was circulated through the anode compartment of the electrolyzer with the constant flow rate of 30 ml/min *via* a peristaltic pump, while CO_2 was supplied to the cathode side with a constant flow rate of 10 standard cubic centimeters per minute (sccm). After three-minutes of initial operation, a full-cell potential of -3.0 V was applied to the electrolyzer and the potential then was gradually increased with increments of -0.10 V or -0.05 V. The current was stabilized for 15-20 min between two voltage increments.

CO_2-to-C_2H_4 measurements in the cascade MEA system

An Ag electrode was used to convert CO_2 into CO in 0.1M $KHCO_3$ solution. The MEA cell possessed the same geometric active area of 4 cm^2. The first MEA setup was operated at -3.8 V with a CO_2 inlet flow rate of 10 sccm. The outlet of the first MEA setup was connected to a

CO_2 capture solution using a 30 wt % ethanolamine aqueous solution. Purified CO was then supplied to the second MEA cell for conversion of CO to C_2H_4. 1 M KOH was used as the anolyte, and the CO-to-ethylene conversion was evaluated at different potentials from -2.0 to -3.0 V.

Quantification of the CO_2RR products. The electrochemical data were recorded while simultaneously collecting the CO_2RR gas products by using an automatic sampler connected to the cathode outlet. A cold trap was used a collect the liquid products before the sampler. For each applied potential, the gas products were collected at least 3 times with proper time intervals. The gas alliquots were then injected into an online gas chromatograph (Agilent, Micro GC-490) equipped with a TCD detector and Molsieve 5A column continuously. Hydrogen and argon (99.9999%) were used as the carrier gases. Liquid products were quantified by 1H NMR spectroscopy (600 Mhz Avance III Bukrer with a cryorobe Prodigy TCI) using deionized water with 0.1 % (w/w) of DSS (Sodium trimethylsilylpropanesulfonate) like internal standard for the quantification of the ethanol and formate. An 1D sequence water suppression with excitation sculpting with gradients(zgesgp) was used for the acquisition (Number of scan = 32, Delay D1=30 s). Owing to the liquid product crossover, the FE values of the liquid products were calculated based on the total amount of the products collected on the anode and cathode sides during the same period.

Stability measurements in the MEA configuration. For the stability tests, the MEA electrolyzer was operated at a constant voltage of -3.55 V with a continuous feed in CO_2. The gas products were collected at frequent time intervals and FE values were calculated from the average value obtained from three successive injections. As for the liquid products, the total liquid products were collected at the end of the experiments.

Faradaic Efficiency, Selectivity, Energy Efficiency and Energy power consumption Calculations. The Faradaic efficiency (FE, %) of each gas product was calculated as follows:

$$FE_{gas} = g_i \times v \times \frac{z_i}{RT} FP_0 \times \frac{1}{I_{total}} \times 100\% \qquad (5)$$

The Faradaic efficiency (FE, %) of each liquid product was calculated as follows:

$$FE_{liquid} = l_i \times \frac{z_i}{Q_{total}} F \times 100\% \qquad (6)$$

The formation rate (R) for each species(i) was calculated as follows:

$$R_i = \frac{Q_{total} \times FE_i}{96485 \times z_i \times t \times S} \qquad (7)$$

The single-pass conversion rate (SPC, %) of CO_2 to C_2H_4 was calculated as follows:

$$SPC = \frac{C_{C2H4} \times flow\ rate_{outlet}}{C_{CO2} \times flow\ rate_{inlet}} \times 100 \qquad (8)$$

The full-cell energy efficiencies (EE, %) was calculated as follows:

$$EE = \frac{(1.23 - E_i) \times FE_i}{E_{cell}} \qquad (9)$$

The selectivity (%) of ethylene was calculated as follows:

$$Selectivity_{C2H4} = \frac{2R_{C2H4}}{R_{CO} + R_{HCOOH} + 2R_{C2H4} + 2R_{C2H5OH}} \qquad (10)$$

The electrical power consumption (EPC, kWh) characterizes the amount of electric energy (typically expressed in kWh) that is required for producing 1 Nm^3 of product gas, and it was calculated as follows:

$$EPC = \frac{E_{cell} \times n \times F}{FE \times V_m} \qquad (11)$$

where g_i represents the volume fraction of gas product i; v represents the gas flow rate at the outlet in sccm; z_i represents the number of electrons required to produce one molecule of product i; I_{total} represents the total current; l_i represents the number of moles of liquid product i; Q_{total} represents the charge passed while the liquid products are being collected; C_{C2H4} and C_{CO2} represents the concentrations of C_2H_4 and CO_2 measured by online GC. P_0 = 1.01 × 10 5 Pa, T = 273.15 K, F = 96,485 C mol^{-1} and R = 8.314 $Jmol^{-1}K^{-1}$; t represents the electrolysis time (h); S represents the geometric area of the electrode (cm^2); E_i represents the thermodynamic potential (versus RHE) for CO_2RR to species i and E_{cell} represents the cell voltage in two-electrode setup (-1.15 V for CO_2-to-C_2H_4, and -1.06 V for CO-to-C_2H_4); V_m is the molar volume of ideal gas under normal conditions.

Acknowledgments

D.V., H. W. and K.Q. acknowledge funding from the European Research Council (ERC) under

the European Union's Horizon 2020 research and innovation programme (grant agreement no. 804320). The authors acknowledge the use of TEM instrumentation provided by the National Facility ELECMI ICTS ("Division de Microscopia Electronica", Universidad de Cadiz, DME-UCA). L.L. acknowledges funding from the European Union's Horizon 2020 research and innovation program (grant agreement 823717-ESTEEM3) and the Spanish Ministerio de Economia y Competitividad (PID2019-107578GA-I00), the Ministerio de Ciencia e Innovación MCIN/AEI/10.13039/501100011033, and the European Union "NextGenerationEU"/PRTR (RYC2021-033764-I, CPP2021-008986). C.S. acknowledged funding from the French National Agency (ANR, JCJC program, MONOMEANR-20-CE08-0009). The authors acknowledge Martina Rüscher, Felix T. Haase and Lichen Bai for their help on synchrotron tests. We acknowledge SOLEIL for provision of synchrotron radiation facilities and we would like to thank Andrea Zitolo for assistance in using beamline SAMBA within the proposal 20200732. XAS experiments were also performed at CLAESS beamline at ALBA synchrotron with the collaboration of ALBA staff. Patrice Montels and Daniel Valenza are acknowledged for their technical assistance with the MEA cells.

References

1 Bushuyev, O. S. *et al.* What should we make with CO_2 and how can we make it? *Joule* **2**, 825-832 (2018).

2 Ager, J. W. & Lapkin, A. A. Chemical storage of renewable energy. *Science* **360**, 707-708 (2018).

3 Jouny, M., Luc, W. & Jiao, F. General techno-economic analysis of CO_2 electrolysis systems. *Industrial & Engineering Chemistry Research* **57**, 2165-2177 (2018).

4 Verma, S., Kim, B., Jhong, H. R. M., Ma, S. & Kenis, P. J. A gross-margin model for defining technoeconomic benchmarks in the electroreduction of CO_2. *ChemSusChem* **9**, 1972-1979 (2016).

5 Verma, S., Lu, S. & Kenis, P. J. Co-electrolysis of CO_2 and glycerol as a pathway to carbon chemicals with improved technoeconomics due to low electricity consumption. *Nature Energy* **4**, 466-474 (2019).

6 Li, F. *et al.* Molecular tuning of CO_2-to-ethylene conversion. *Nature* **577**, 509-513 (2020).

7 García de Arquer, F. P. *et al.* CO_2 electrolysis to multicarbon products at activities greater than 1 A cm− 2. *Science* **367**, 661-666 (2020).

8 Zhong, M. *et al.* Accelerated discovery of CO_2 electrocatalysts using active machine learning. *Nature* **581**, 178-183 (2020).

9 Liu, W. *et al.* Electrochemical CO2 reduction to ethylene by ultrathin CuO nanoplate arrays. *Nature communications* **13**, 1877 (2022).

10 Ma, S., Luo, R., Moniri, S., Lan, Y. & Kenis, P. J. Efficient electrochemical flow system with improved anode for the conversion of CO_2 to CO. *Journal of The Electrochemical Society* **161**, F1124 (2014).
11 Verma, S., Lu, X., Ma, S., Masel, R. I. & Kenis, P. J. The effect of electrolyte composition on the electroreduction of CO_2 to CO on Ag based gas diffusion electrodes. *Physical Chemistry Chemical Physics* **18**, 7075-7084 (2016).
12 Dinh, C.-T. *et al.* CO_2 electroreduction to ethylene via hydroxide-mediated copper catalysis at an abrupt interface. *Science* **360**, 783-787 (2018).
13 Weng, L.-C., Bell, A. T. & Weber, A. Z. Towards membrane-electrode assembly systems for CO_2 reduction: a modeling study. *Energy & Environmental Science* **12**, 1950-1968 (2019).
14 Jouny, M., Hutchings, G. S. & Jiao, F. Carbon monoxide electroreduction as an emerging platform for carbon utilization. *Nature Catalysis* **2**, 1062-1070 (2019).
15 Xiao, H., Goddard, W. A., Cheng, T. & Liu, Y. Cu metal embedded in oxidized matrix catalyst to promote CO_2 activation and CO dimerization for electrochemical reduction of CO_2. *Proceedings of the National Academy of Sciences* **114**, 6685-6688 (2017).
16 De Luna, P. *et al.* Catalyst electro-redeposition controls morphology and oxidation state for selective carbon dioxide reduction. *Nature Catalysis* **1**, 103-110 (2018).
17 Arán-Ais, R. M., Scholten, F., Kunze, S., Rizo, R. & Roldan Cuenya, B. The role of in situ generated morphological motifs and Cu (i) species in C_{2+} product selectivity during CO_2 pulsed electroreduction. *Nature Energy* **5**, 317-325 (2020).
18 Eilert, A., Roberts, F. S., Friebel, D. & Nilsson, A. Formation of copper catalysts for CO_2 reduction with high ethylene/methane product ratio investigated with in situ X-ray absorption spectroscopy. *The journal of physical chemistry letters* **7**, 1466-1470 (2016).
19 Zhou, Y. *et al.* Dopant-induced electron localization drives CO_2 reduction to C_2 hydrocarbons. *Nature chemistry* **10**, 974-980 (2018).
20 Lee, S., Kim, D. & Lee, J. Electrocatalytic production of C_3-C_4 compounds by conversion of CO_2 on a chloride-induced bi-phasic Cu_2O-Cu catalyst. *Angewandte Chemie* **127**, 14914-14918 (2015).
21 Cao, L., Wu, Y., Hang, T. & Li, M. Covalent Grafting of Dielectric Films on Cu (111) Surface via Electrochemical Reduction of Aryl Diazonium Salts. *Langmuir* **38**, 14969-14980 (2022).
22 Pinson, J. Attachment of organic layers to materials surfaces by reduction of diazonium salts. *Aryl diazonium salts*, 1-35 (2012).
23 Berisha, A., Chehimi, M. M., Pinson, J. & Podvorica, F. Electrode surface modification using diazonium salts. *Electroanalytical Chemistry* **26** (2015).
24 Hollins, P. The influence of surface defects on the infrared spectra of adsorbed species. *Surface Science Reports* **16**, 51-94 (1992).
25 Belanger, D. & Pinson, J. Electrografting: a powerful method for surface modification. *Chemical Society Reviews* **40**, 3995-4048 (2011).
26 Mooste, M. *et al.* Surface and electrochemical characterization of aryl films grafted on polycrystalline copper from the diazonium compounds using the rotating disk electrode method. *Journal of Electroanalytical Chemistry* **817**, 89-100 (2018).
27 Kendig, M., Hon, M. & Sinko, J. Inhibition of Oxygen Reduction on Copper in Neutral Sodium Chloride. *ECS Transactions* **1**, 119 (2006).
28 Chira, A., Bucur, B. & Radu, G.-L. Electrodeposited organic layers formed from aryl diazonium salts for inhibition of copper corrosion. *Materials* **10**, 235 (2017).
29 Li, D. *et al.* Surface functionalization of nanomaterials by aryl diazonium salts for biomedical sciences. *Advances in Colloid and Interface Science* **294**, 102479 (2021).
30 Gillan, L., Teerinen, T., Johansson, L.-S. & Smolander, M. Controlled diazonium electrodeposition towards a biosensor for C-reactive protein. *Sensors International* **2**, 100060 (2021).
31 Hetemi, D., Noël, V. & Pinson, J. Grafting of diazonium salts on surfaces: Application to biosensors. *Biosensors* **10**, 4 (2020).

32 Mahouche-Chergui, S., Gam-Derouich, S., Mangeney, C. & Chehimi, M. M. Aryl diazonium salts: a new class of coupling agents for bonding polymers, biomacromolecules and nanoparticles to surfaces. *Chemical Society Reviews* **40**, 4143-4166 (2011).
33 Wei, G. *et al*. Covalent modification of reduced graphene oxide by means of diazonium chemistry and use as a drug-delivery system. *Chemistry–A European Journal* **18**, 14708-14716 (2012).
34 Hammett, L. P. The effect of structure upon the reactions of organic compounds. Benzene derivatives. *Journal of the American Chemical Society* **59**, 96-103 (1937).
35 Hansch, C., Leo, A. & Taft, R. A survey of Hammett substituent constants and resonance and field parameters. *Chemical reviews* **91**, 165-195 (1991).
36 Li, Y. C. *et al*. Binding site diversity promotes CO_2 electroreduction to ethanol. *Journal of the American Chemical Society* **141**, 8584-8591 (2019).
37 Goodpaster, J. D., Bell, A. T. & Head-Gordon, M. Identification of possible pathways for C–C bond formation during electrochemical reduction of CO_2: new theoretical insights from an improved electrochemical model. *The journal of physical chemistry letters* **7**, 1471-1477 (2016).
38 Montoya, J. H., Peterson, A. A. & Nørskov, J. K. Insights into C-C Coupling in CO_2 Electroreduction on Copper Electrodes. *ChemCatChem* **5**, 737-742 (2013).
39 Cheng, T., Xiao, H. & Goddard III, W. A. Free-energy barriers and reaction mechanisms for the electrochemical reduction of CO on the Cu (100) surface, including multiple layers of explicit solvent at pH 0. *The journal of physical chemistry letters* **6**, 4767-4773 (2015).
40 Filhol, J. S. & Neurock, M. Elucidation of the electrochemical activation of water over Pd by first principles. *Angewandte Chemie* **118**, 416-420 (2006).
41 Neugebauer, J. & Scheffler, M. Adsorbate-substrate and adsorbate-adsorbate interactions of Na and K adlayers on Al (111). *Physical Review B* **46**, 16067 (1992).
42 Hurley, B. L. & McCreery, R. L. Covalent bonding of organic molecules to Cu and Al alloy 2024 T3 surfaces via diazonium ion reduction. *Journal of The Electrochemical Society* **151**, B252 (2004).
43 Doppelt, P., Hallais, G., Pinson, J., Podvorica, F. & Verneyre, S. Surface modification of conducting substrates. Existence of azo bonds in the structure of organic layers obtained from diazonium salts. *Chemistry of Materials* **19**, 4570-4575 (2007).
44 Menanteau, T., Dias, M. n., Levillain, E., Downard, A. J. & Breton, T. Electrografting via diazonium chemistry: the key role of the aryl substituent in the layer growth mechanism. *The Journal of Physical Chemistry C* **120**, 4423-4429 (2016).
45 Cai, J. *et al*. Chemical grafting of the superhydrophobic surface on copper with hierarchical microstructure and its formation mechanism. *Applied Surface Science* **436**, 950-956 (2018).
46 Kusoglu, A. & Weber, A. Z. New insights into perfluorinated sulfonic-acid ionomers. *Chemical reviews* **117**, 987-1104 (2017).
47 Allen, F. I. *et al*. Morphology of hydrated as-cast Nafion revealed through cryo electron tomography. *ACS Macro Letters* **4**, 1-5 (2015).
48 Kreuer, K. D. & Portale, G. A critical revision of the nano-morphology of proton conducting ionomers and polyelectrolytes for fuel cell applications. *Advanced Functional Materials* **23**, 5390-5397 (2013).
49 Ozden, A. *et al*. High-rate and efficient ethylene electrosynthesis using a catalyst/promoter/transport layer. *ACS Energy Letters* **5**, 2811-2818 (2020).
50 Li, J. *et al*. Silica-copper catalyst interfaces enable carbon-carbon coupling towards ethylene electrosynthesis. *Nature communications* **12**, 1-10 (2021).
51 Wang, Y. *et al*. Catalyst synthesis under CO_2 electroreduction favours faceting and promotes renewable fuels electrosynthesis. *Nature Catalysis* **3**, 98-106 (2020).
52 Lee, W. H. *et al*. Highly selective and stackable electrode design for gaseous CO_2 electroreduction to ethylene in a zero-gap configuration. *Nano Energy* **84**, 105859

(2021).
53 Zhang, T. *et al.* Highly selective and productive reduction of carbon dioxide to multicarbon products via in situ CO management using segmented tandem electrodes. *Nature Catalysis* **5**, 202-211 (2022).
54 Chen, X. *et al.* Electrochemical CO_2-to-ethylene conversion on polyamine-incorporated Cu electrodes. *Nature Catalysis* **4**, 20-27 (2021).
55 Zhang, W. *et al.* Atypical oxygen-bearing copper boosts ethylene selectivity toward electrocatalytic CO_2 reduction. *Journal of the American Chemical Society* **142**, 11417-11427 (2020).
56 An, H. *et al.* Sub-Second Time-Resolved Surface-Enhanced Raman Spectroscopy Reveals Dynamic CO Intermediates during Electrochemical CO_2 Reduction on Copper. *Angewandte Chemie International Edition* **60**, 16576-16584 (2021).
57 Gunathunge, C. M. *et al.* Spectroscopic observation of reversible surface reconstruction of copper electrodes under CO_2 reduction. *The Journal of Physical Chemistry C* **121**, 12337-12344 (2017).
58 Gunathunge, C. M., Ovalle, V. J., Li, Y., Janik, M. J. & Waegele, M. M. Existence of an electrochemically inert CO population on Cu electrodes in alkaline pH. *ACS Catalysis* **8**, 7507-7516 (2018).
59 Gunathunge, C. M., Li, J., Li, X., Hong, J. J. & Waegele, M. M. Revealing the Predominant Surface Facets of Rough Cu Electrodes under Electrochemical Conditions. *ACS Catalysis* **10**, 6908-6923 (2020).
60 Gunathunge, C. M., Ovalle, V. J. & Waegele, M. M. Probing promoting effects of alkali cations on the reduction of CO at the aqueous electrolyte/copper interface. *Physical Chemistry Chemical Physics* **19**, 30166-30172 (2017).
61 Heyes, J., Dunwell, M. & Xu, B. CO_2 reduction on Cu at low overpotentials with surface-enhanced in situ spectroscopy. *The Journal of Physical Chemistry C* **120**, 17334-17341 (2016).
62 Akemann, W. & Otto, A. Vibrational modes of CO adsorbed on disordered copper films. *Journal of Raman spectroscopy* **22**, 797-803 (1991).
63 Verma, S. *et al.* Insights into the low overpotential electroreduction of CO_2 to CO on a supported gold catalyst in an alkaline flow electrolyzer. *ACS Energy Letters* **3**, 193-198 (2017).
64 Xiao, H., Cheng, T., Goddard III, W. A. & Sundararaman, R. Mechanistic explanation of the pH dependence and onset potentials for hydrocarbon products from electrochemical reduction of CO on Cu (111). *Journal of the American Chemical Society* **138**, 483-486 (2016).
65 Yadegari, H. *et al.* Glycerol Oxidation Pairs with Carbon Monoxide Reduction for Low-Voltage Generation of C_2 and C_3 Product Streams. *ACS Energy Letters* **6**, 3538-3544 (2021).
66 Ozden, A. *et al.* Cascade CO_2 electroreduction enables efficient carbonate-free production of ethylene. *Joule* **5**, 706-719 (2021).
67 Voiry, D. *et al.* High-quality graphene via microwave reduction of solution-exfoliated graphene oxide. *Science* **353**, 1413-1416 (2016).
68 Ripatti, D. S., Veltman, T. R. & Kanan, M. W. Carbon monoxide gas diffusion electrolysis that produces concentrated C_2 products with high single-pass conversion. *Joule* **3**, 240-256 (2019).
69 Rabinowitz, J. A. & Kanan, M. W. The future of low-temperature carbon dioxide electrolysis depends on solving one basic problem. *Nature Communications* **11**, 1-3 (2020).
70 Gabardo, C. M. *et al.* Continuous carbon dioxide electroreduction to concentrated multi-carbon products using a membrane electrode assembly. *Joule* **3**, 2777-2791 (2019).
71 Perdew, J. P., Burke, K. & Ernzerhof, M. Generalized gradient approximation made simple. *Physical review letters* **77**, 3865 (1996).

72 Blöchl, P. E. Projector augmented-wave method. *Physical review B* **50**, 17953 (1994).
73 Paier, J., Hirschl, R., Marsman, M. & Kresse, G. The Perdew–Burke–Ernzerhof exchange-correlation functional applied to the G2-1 test set using a plane-wave basis set. *The Journal of chemical physics* **122**, 234102 (2005).
74 Grimme, S., Ehrlich, S. & Goerigk, L. Effect of the damping function in dispersion corrected density functional theory. *Journal of computational chemistry* **32**, 1456-1465 (2011).
75 Henkelman, G., Arnaldsson, A. & Jónsson, H. A fast and robust algorithm for Bader decomposition of charge density. *Computational Materials Science* **36**, 354-360 (2006).
76 Henkelman, G., Uberuaga, B. P. & Jónsson, H. A climbing image nudged elastic band method for finding saddle points and minimum energy paths. *The Journal of chemical physics* **113**, 9901-9904 (2000).
77 Montoya, J. H., Shi, C., Chan, K. & Nørskov, J. K. Theoretical insights into a CO dimerization mechanism in CO_2 electroreduction. *The journal of physical chemistry letters* **6**, 2032-2037 (2015).
78 Nørskov, J. K. *et al.* Origin of the overpotential for oxygen reduction at a fuel-cell cathode. *The Journal of Physical Chemistry B* **108**, 17886-17892 (2004).

Author Contributions

D.V. conceived the idea, designed the experiments. D.R. performed the DFT calculations and discussed the results with D.V. and H.W.. H.W. designed the experiments with D.V., prepared the electrodes and performed the electrochemical measurements. H.W., D.R. and D.V. analyzed the data and wrote the manuscript. L. H. and V.F. performed the XPS and Auger measurements and analyzed the data with H.W.. J.T. and H.W. performed the *ex-situ* and *operando* XAS measurements and analyzed the data. L.L. performed high-resolution STEM, TEM and EELS on the Cu-X catalysts and discussed the results with H.W. and D.V.. S. Y. performed DFT data collections and discussed the results with H.W.. E.P. carried out the liquid NMR spectroscopy measurements. K.Q., Y.Z., assisted H.W. with the electrochemical investigations and the GC analyses. W.W., J. Li and J. Jiu assisted H.W. with the physical characterization of the samples and the *operando* Raman measurements. C.S. and P. M. discussed the electrocatalytic performance with H.W. and D.V.. B.R.C. discussed the XAS data with J.T., H.W. and D.V. All of the authors edited the manuscript before submission.

Data availability

The data that support the plots and other findings in this study are available from the

corresponding authors upon reasonable request.

Competing financial interests

The authors declare no competing financial interests.

Additional Information

Supplementary information and chemical compound information are available in the online version of the paper.

Correspondence and requests for materials should be addressed to D.V. (damien.voiry@umontpellier.fr) and D. R. (dewei@ujs.edu.cn)

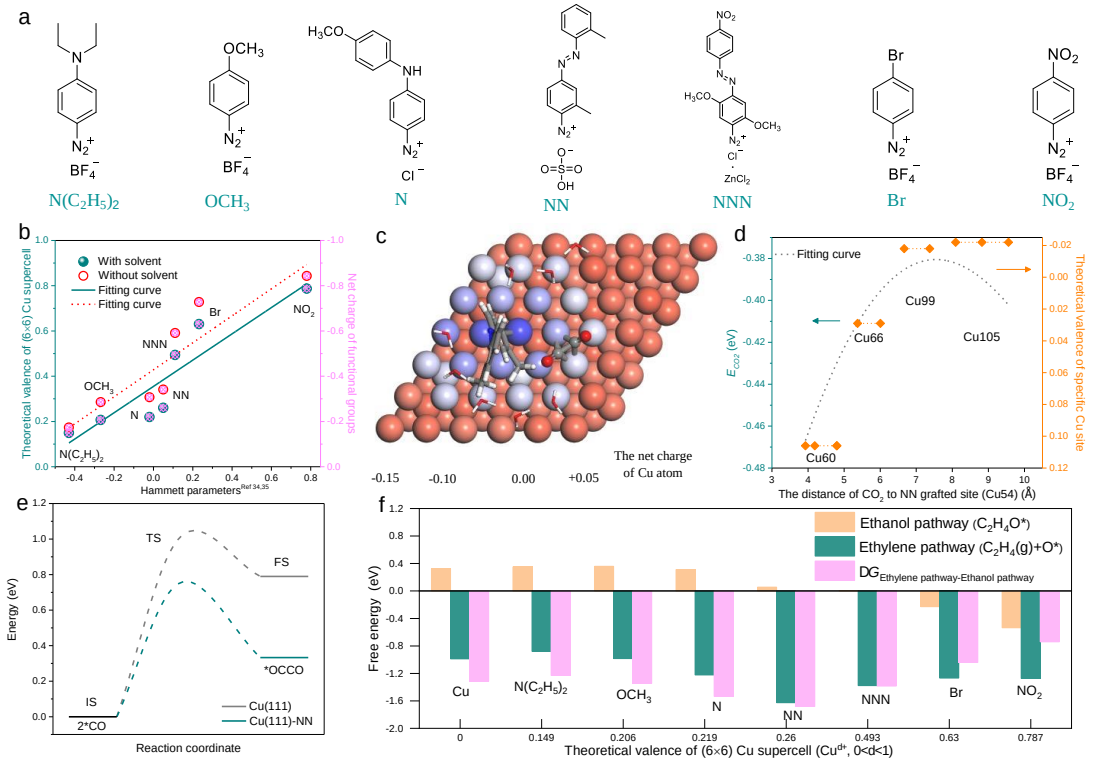

Fig. 1 Density functional theory calculations. (a) Molecular structures of different diazonium salts. **(b)** The relationship between the theoretical valence of the whole (6×6) Cu supercell and the electro-withdrawing ability of different substitutes on phenyl according to Hammett

parameters[34,35]. **(c)** Heat map of the valence of the top Cu atoms near the NN functional group calculated considering explicit water. Cu, N, C and O atoms are illustrated as orange, blue, grey and red balls, respectively, while water molecules and NN are shown as lines. (**d**) The relationship between the distance of adsorbed CO_2 to the NN grafted copper atom (Cu54), the theoretical valence of CO_2-adsorbed specific Cu sites (Cu60, Cu66, Cu99 and Cu105) and the related CO_2 adsorption energy on CO_2-adsorbed Cu sites. (**e**) Energy profiles for initial states (ISs), transition states (TSs), and final states (FSs) of CO dimerization on Cu (111) and Cu (111)-NN. (**f**) Gibbs free energy difference associated with the ethylene and ethanol pathways on Cu-X (X refers to NO_2, Br, NNN, NN, N, OCH_3 and $N(C_2H_5)_2$ functional groups), respectively.

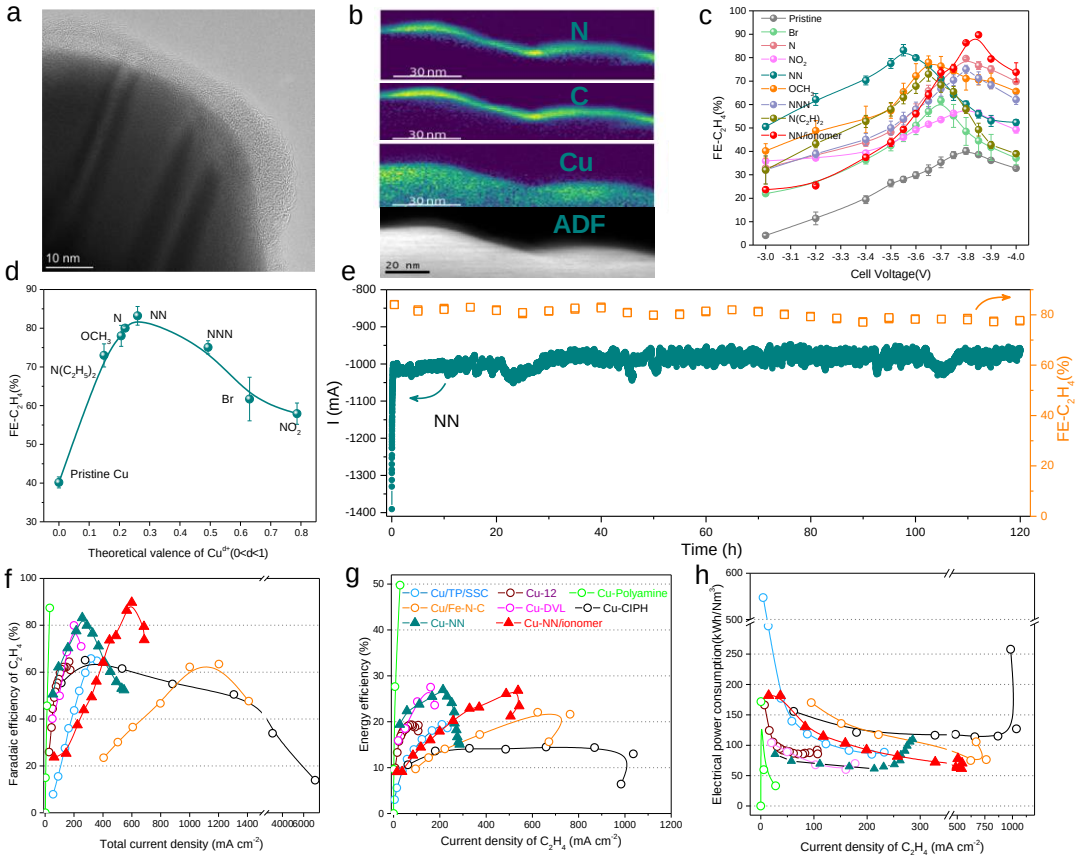

Fig. 2 Structural, compositional and CO_2RR performance for the different Cu-X catalysts measured in MEA flow cells. X refers to NO_2, Br, NNN, NN, N, OCH_3 and $N(C_2H_5)_2$ functional groups. **(a)** HR-TEM image, (**b**) the corresponding N, C and Cu EELS elemental maps and corresponding ADF image taken from a section of Cu surface on the NN-

functionalized Cu electrode. (**c**) Comparison of FEs for ethylene on the different Cu electrodes measured at full-cell potentials ranging from -3.0 to −4.0 V and measured in 0.5 M $KHCO_3$. (**d**) The relationship between FE_{C2H4} and the theoretical valences of the Cu sites on the different catalysts. (**e**) CO_2RR performance of NN-Cu at a full-cell potential of -3.55 V and with a 10 sccm feed in CO_2 over 120 hours. The anolyte consisted in a 0.5 M $KHCO_3$ solution circulating at a flow rate of 30 ml min^{-1}. The blue line represents the current recorded during the extended CO_2RR experiment (primary *y* axis). The empty orange symbols represent the FE for C_2H_4 averaged from three independent measurements (secondary *y* axis). Comparison of the selectivity (**f**), energy efficiency (**g**) and electric power consumption (**h**) for C_2H_4 based measured on the different Cu-X cathodes with literature benchmarks for MEA electrolyzers. For each reference (Cu-12, Cu-CIPH, Cu/Fe-N-C, Cu-Polyamine, Cu/TP/SSC and Cu-DVL catalysts), the plotted values are those corresponding to the reported best performance[6,7,9,49,53,54] (Supplementary Table 17). The error bars in **c** and **d** correspond to the standard deviation of three independent measurements.

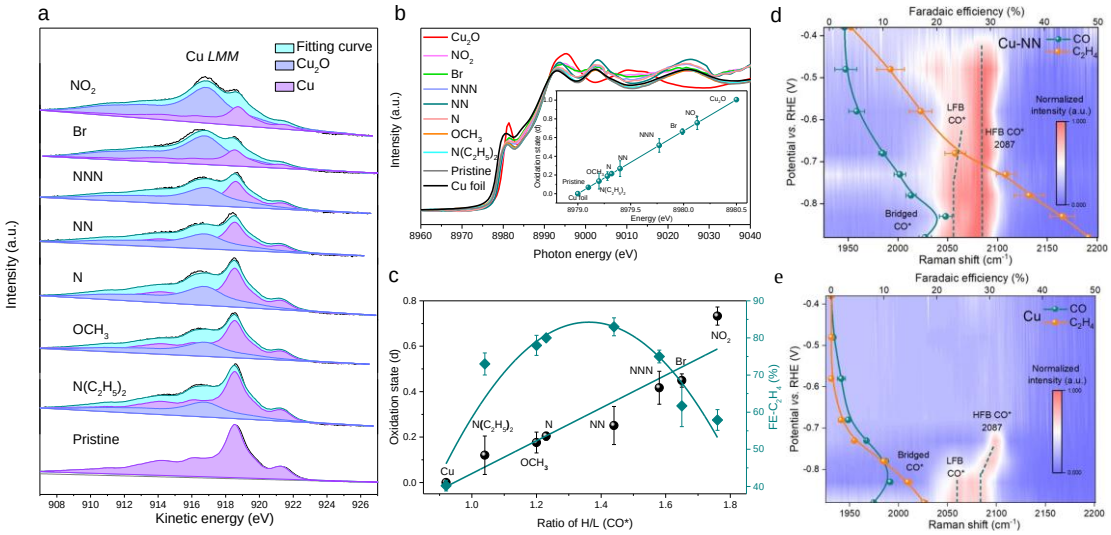

Fig. 3 XAS, Auger and *operando* Raman characterizations. (a) The copper *LMM* Auger spectra of the Cu-X electrodes. The amounts of Cu_2O and Cu contributions were estimated from the integrated area of the corresponding curves. **(b)** Copper K-edge XANES spectra of Cu-X catalysts after being electrochemically reduced. Inset: average oxidation state of copper in Cu-X obtained from copper K-edge XANES. The edge position of each sample is determined from the intercept of the main edge and pre-edge contributions. The error bars represent the standard deviation of three separate measurements for each sample. **(c)** The relationship between the FE for ethylene, the oxidation state of copper in Cu-X and the ratio of H/L-*CO obtained from the *operando* Raman spectra of the Cu-X electrodes at -0.88 V versus RHE. H and L refer high frequency and low frequency modes. **(d)** The correlations between the FE_{CO}, the FE_{C2H4} and the *operando* Raman heatmaps of Cu-NN electrode and pristine Cu measured from -0.88 V to -0.38 V *vs.* RHE. Only the CO region is examined here (1900-2200 cm^{-1}). The error bars in **b**, **c**, **d** and **e** correspond to the standard deviation of three independent measurements.

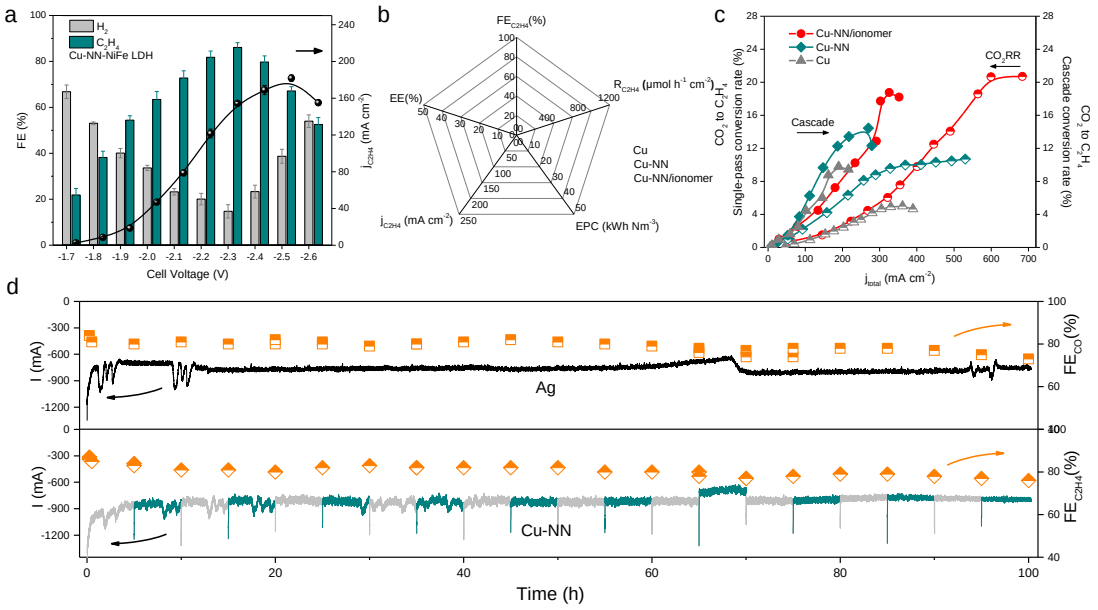

Fig. 4 CO_2-to-C_2H_4 performance in the cascade flow process. (a) The FE for C_2H_4 obtained using CO as feed. (**b**) Comparison of different performance of the Cu-X electrodes: Faradaic efficiency (FE), energy efficiency (EE), specific current density (j), energy power consumption (EPC) and formation rate (R) of C_2H_4. (**c**) Comparison of the CO_2-to-C_2H_4 single-pass conversion measured for a single MEA cell (half-filled sphere) and for the cascade flow process (filled sphere). (**d**) The stability of Ag and Cu-NN catalysts in MEA cells. The error bars in **a** and **c** correspond to the standard deviation of three independent measurements.

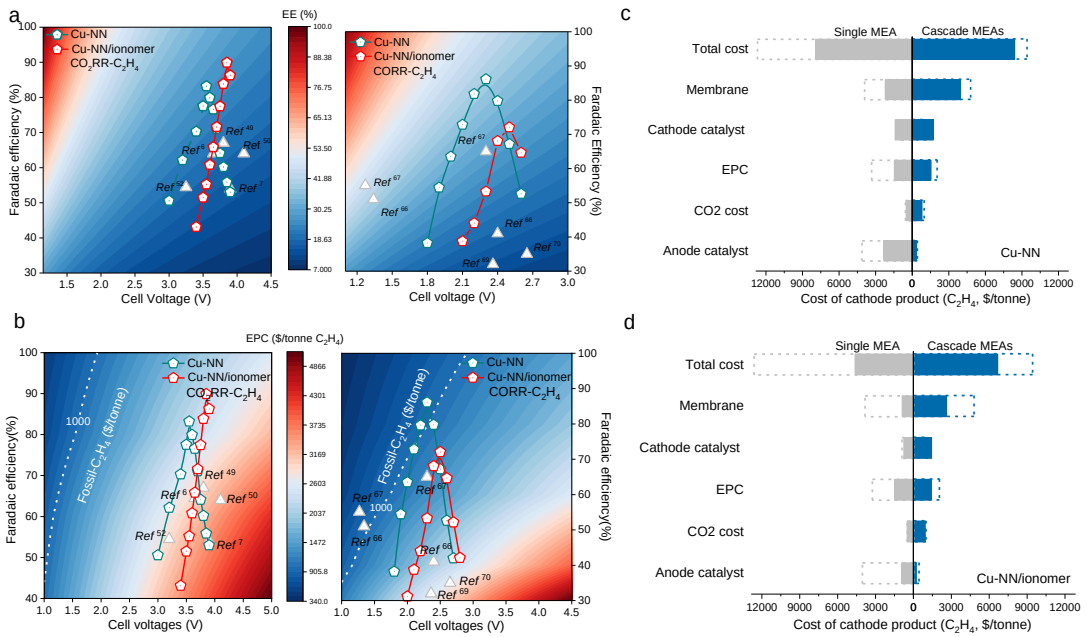

Fig. 5 Techno-economic analyses for the CO_2-to-C_2H_4 conversion based on the direct and the cascade flow processes. The comparison of energy efficiency (EE) (**a**) and the cost of the electrical power consumption (**b**) for the CO_2-to-C_2H_4 and the CO-to-C_2H_4 reactions. Comparison of operational costs for production of C_2H_4 on Cu-NN(**c**) and Cu-NN/ionomer(**d**) in both single MEA and cascade MEA systems (the dash line refers to pristine Cu).